Effect of interfacial roughness on thermal boundary conductance: An elastic wave model using the Kirchhoff approximation

Bin Liu [a], Vladimir I. Khvesyuk [a], Alexander A. Barinov [a], Moran Wang [b,*]

[a] *Department of Thermophysics, Bauman Moscow State Technical University, Moscow 105005, Russia*
[b] *Key Laboratory for Thermal Science and Power Engineering of Ministry of Education, Department of Engineering Mechanics and CNMM, Tsinghua University, Beijing 100084, China*

ARTICLE INFO

ABSTRACT

Interfacial roughness plays an important role in nanoscale thermal transport, while this issue still lacks a theoretical description due to the difficulty in quantifying the phonon scattering at the disordered interface. We report an elastic wave model (EWM) that describes the phonon–interface interaction by the interface elasticity. The transmissivity calculation based on the interfacial displacement and stress continuity incorporates the mode conversion and nonlinear vibration spectra of phonon waves, and the resulting cut-off frequency. Compared with the acoustic mismatch model that also assumes specular scattering of phonons waves, the applicable range of EWM is extended to room temperature and shows better accuracy. Based on this model, we use a statistical method with the Kirchhoff approximation and introduce the tangent plane slope distribution to determine the phonon scattering at a Gaussian-distributed rough interface. And the effective transmission coefficient is calculated by integrating the contributions of all points to the energy transmission. Calculated thermal boundary conductance (TBC) by a Landauer formula agrees well with the experiments of Al/SiO$_2$/Si and Au/SiO$_2$/Si rough interfaces. And the results show that the TBC of interface with sub-nanometer RMS roughness (10^{-10} m) is close to that of the smooth interface. After this transition, the increasing σ can significantly impact the interfacial heat transfer. Compared with existing models, the EWM can quantitatively estimate the effect of roughness on TBC and give a transmission image of wave-like phonons at the interface. This work contributes to an in-depth understanding of phonon wave effects in nanostructures.

1. Introduction

Interfacial heat transfer is essential and strongly affects the overall thermal performance in many applications, e.g., integrated circuits, multilayer thin films, superlattice structures, and other nanostructured materials [1–4]. The efficiency of interfacial heat transfer is described by the thermal boundary conductance (TBC), which is defined as the ratio of the heat flow per unit area across the interface to the temperature difference [5]. Previous works have demonstrated how the interfacial factors, such as interfacial chemistry and bonding [6], interlayer [7,8], mismatch of phonon spectra [9], and interfacial roughness [10–12], can respectively influence the TBC. Among them, interfacial roughness due to atomic disorder and defects commonly exists at interfaces and generates a significant source of thermal resistance.

In recent years, several TBC studies have focused on interface properties that have a greater impact on thermal transport even than material mismatch under certain conditions [13–18]. Experimentally, the interfacial roughness can be controlled by interfacial processing methods, e.g., chemical etching [15,19], quantum-dot patterning [14], and

interfacial-misfit array growth [20]. The surface roughness changes the phonon transport mechanism in nanostructures by enhancing phonon–interface scattering, which has been confirmed by molecular dynamics simulations [21–23]. And the acoustic mismatch model (AMM) and diffuse mismatch model (DMM) are commonly used to estimate the phonon-dominated heat transfer at the interface [5,24], while they fail to evaluate the effect of interfacial roughness on the TBC due to their limit assumptions of phonons: complete specular scattering and complete diffuse scattering, respectively. Despite the importance of interfacial roughness, a void exists in the current knowledge of how phonons interact with rough interfaces, and there is still a lack of corresponding theoretical models that interpret the thermal transport mechanism.

Moreover, wave scattering at rough surfaces has been extensively studied in optics and acoustics. The influence of interfacial roughness on the wave behavior of thermal phonons is also important in nanostructured materials [25,26]. For instance, the superlattice is a good

---

candidate for thermoelectric conversion materials, owing to its low thermal conductivity. A number of studies demonstrate that the low thermal conductivities of superlattices are due to phonon scattering at interfaces caused by interfacial atomic disorder or other defects [22, 25,27]. In addition, novel bandgap materials that allow control of thermal energy transport are based on the wave interference effects of phonons [28], the specular scattering and phase maintaining of phonons are critical for the coherent manipulation of heat, which is currently a topic of great interest [25,29,30]. Although in previous theoretical works advances have been made by treating phonons as particles, the analytical models that explain their wave nature still remain to be expanded [31,32].

This work aims to interpret the heat transfer dominated by phonons at the metal–semiconductor interface by considering the wave characteristics of phonons. We present an elastic wave model (EWM) for predicting the TBC at the rough interface. In this model, the wave scattering is statistically determined by an elastic Kirchhoff (or tangent plane) approximation that is widely used to describe the rough interface profile and wave scattering process [33]. The phonon transmission coefficient α on the tangent plane of each point is estimated by frequency-dependent interfacial displacement and stress continuity conditions, combined with the mode conversion and vibration spectra of phonons. The angle- and frequency-dependent effective α of the entire rough interface is computed, both to examine how phonons transmit across interfaces and to better understand the reduction of heat transfer caused by the roughness. Further, we quantitatively analyze the effect of roughness on amplitude and energy ratios of generated waves to the incident wave, which gives microscopic information about phonon waves. And the discussion of discrepancies between the theory and experimental observations of TBC provides opportunities for future investigation.

2. Theory

The TBC is estimated by summation over all energy carrier bombardment and transmission by using a Landauer formulation [5,34,35]. Assuming equilibrium of heat flow at the interface between solid 1 and solid 2, a simplistic mathematical description of the TBC is given by

$$h_K = \frac{1}{2} \sum_j \int_0^{\omega_c} \int_0^{\pi/2} \hbar \omega v_{g,j}(\omega) \alpha_{1 \to 2,j}(\theta, \omega) D_j(\omega)$$
$$\times \frac{\partial f(\omega, T)}{\partial T} \cos\theta \sin\theta d\theta d\omega, \tag{1}$$

where j is the polarization (or mode), ω is the angular frequency of a given phonon, θ is the angle of incidence relative to the interface normal, ω_c is the cut-off frequency (the maximum phonon frequency transmitted across the interface, which will be discussed in detail below), $\hbar$ is the reduced Planck's constant, $D_j(\omega) = \frac{\omega^2}{2\pi^2 v_{g,j}(\omega) v_{p,j}^2(\omega)}$ is the density of states, where $v_{g,j}$ is the group velocity and $v_{p,j}$ is the phase velocity; $f(\omega, T) = \frac{1}{e^{\hbar \omega / k_B T} - 1}$ is the Bose–Einstein distribution function, k_B is the Boltzmann constant, and $\alpha_{1 \to 2,j}(\theta, \omega)$ is the phonon transmission coefficient from solid 1 to solid 2, which can be calculated according to different assumptions (or models) [3,5].

Determination of the transmission coefficient for rough interfaces poses theoretical challenges in terms of phonon scattering mechanism [19]. Here we describe the phonon–interface interaction by utilizing their wave characteristics that are essential to control the thermal transport processes in semiconductor nanostructures [25,32]. Phonons are dominant heat carriers at the metal–dielectric interface [36,37]. In the long wavelength limit, we can quantify the phonons as elastic waves [38,39] and model the phonon–interface interaction by macroelasticity theory [40]. Moreover, the wave scattering at rough surfaces has received considerable attention in fields, e.g., radar detection, sonar research, and ultrasonic inspection [41].
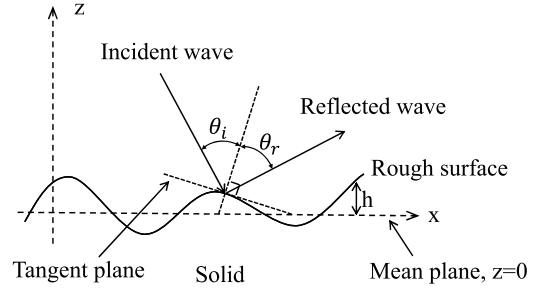

Fig. 1. Wave scattering at a random rough surface in x–z plane. The mean plane $z = 0$ is defined by $<h> = 0$, θ_i and θ_r are the angles of incidence and reflection on the tangent plane, respectively.

2.1. Kirchhoff approximation and rough interface parametrization

We start with the two-dimensional problem of random rough surfaces. In optical and acoustic studies, the typical methods that model the expected scattering are based on the statistics of the surface profile. As shown in Fig. 1, the profile of the rough surface is represented by $z = h(x)$ and h is the deviation of the surface height from the mean plane $z = 0$. The perturbation theory and Kirchhoff approximation are widely used to determine the wave scattering at the rough surface [33, 41]. In the perturbation method the rough surface is regarded as the summation of multi-order perturbations of the mean plane $z = 0$. This method requires that the deviation of the surface h is small compared with the wavelength λ of the incident wave and the surface slope (or gradient) χ is small too [42]. By contrast, the Kirchhoff approximation only requires the restriction on the change rate of the surface slope χ but not limitation on magnitudes of χ and h, which is more appropriate for nanoscale rough interfaces prepared by surface treatment methods. Under the Kirchhoff approximation, it is assumed that any point on the rough surface profile is locally flat and the incident wave is specularly reflected at this point, as shown in Fig. 1. And these points can be called the "specular points" [43,44]. In this case, the wave scattering at a specular point is described by the reflection characteristics on the tangent plane of the point, and the resulting scattered waves are composed of the contributions of all specular points along the interface.

For a rough interface that separates two elastic media by using the Kirchhoff approximation, other details need to be considered. Acoustic systems generally consider a single medium, and the stress-free surface only allows the wave reflection (Fig. 1). At the rough interface, the incident wave will generate both reflected and transmitted waves, and the scattering intensity is related to the elastic properties of the media on both sides of the interface. In an isotropic scattering system, elastic waves have three vibration polarizations (or modes): P — pressure (or longitudinal) wave, SV — shear (or transverse) wave within vertical plane, and SH — shear wave within horizontal plane [40]. Fig. 2 shows a schematic of the scattering system of incident P, SV, and SH waves at the rough interface, the vibration directions of SV and SH waves are parallel and perpendicular to the x–z plane, respectively. We assume that the interface is infinitely thin and separates solid 1 and solid 2. Rigorous consideration of the system includes the mode conversion of waves [40]. The P and SV waves are coupled with each other, and any of them incident at the slip-free interface will generate four waves: two waves are reflected back and two waves are transmitted across the interface. In the process of interfacial scattering, the P and SV waves can be convertible in between [40]. While the incident SH wave only has the displacement components in horizontal direction and generates two waves: reflected SH wave and transmitted SH wave. The difference between elastic waves and acoustic waves mainly comes from the polarization and mode conversion, and these factors are significantly influenced by the interfacial roughness [45].
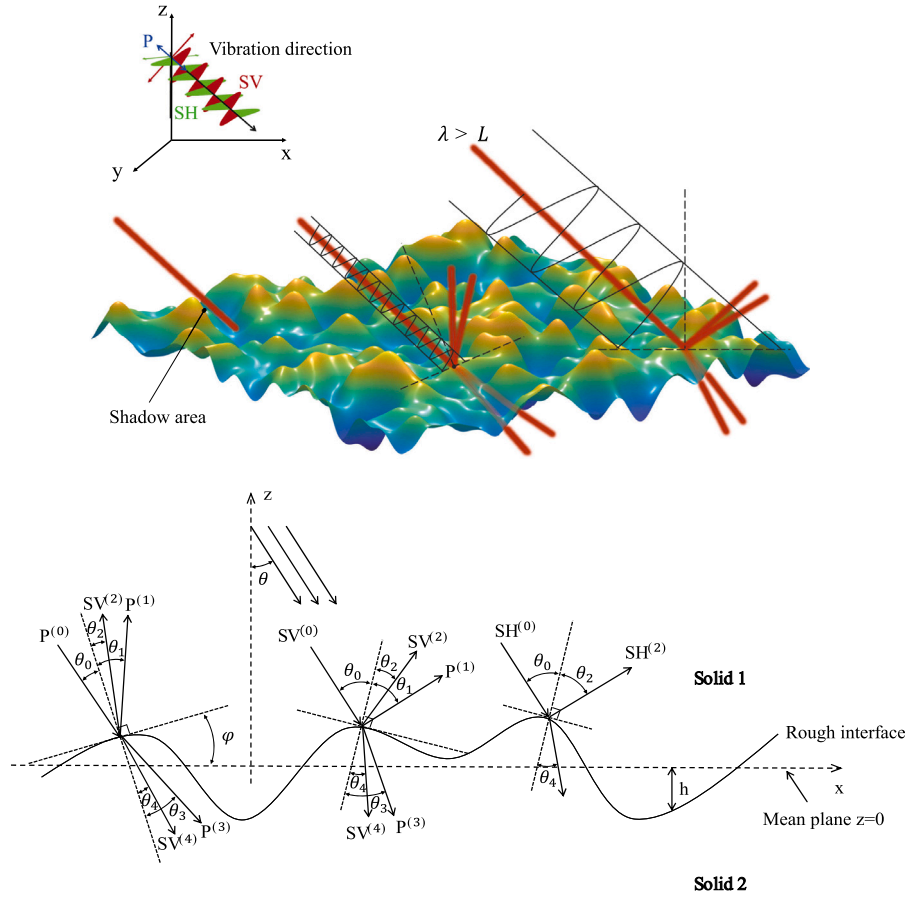
Fig. 2. Reflection and transmission of incident P, SV and SH waves at a random rough interface between two elastic solids. When the wavelength of the incident wave λ is greater than the correlation length L, the rough interface can be regarded as a smooth plane and the incident wave is specularly reflected and transmitted at the mean plane $z = 0$. The superscript (n) represents the type of waves: (0) — incident wave, (1) — reflected pressure wave, (2) — reflected shear wave, (3) — transmitted pressure wave, (4) — transmitted shear wave. θ_n is the angle between the corresponding wave and the tangent plane normal, θ is the angle between the incident wave and the normal to the mean plane $z = 0$, and φ is the angle of inclination of the tangent plane.

The roughness of the interface is evaluated by the statistical description [33,41]. Assuming that the rough interface profile obeys the Gaussian distribution, the probability density function of h is:

$$W_h(h) = \frac{1}{\sqrt{2\pi}\sigma} exp\left(-\frac{h^2}{2\sigma^2}\right), \tag{2}$$

where $\sigma = \sqrt{\langle h^2 \rangle}$ is the root-mean-square (RMS) roughness, which is generally measured as the height parameter of the rough interface in experiments [13–15]. The interface slope χ as the derivative of a normal random function, is also Gaussian-distributed:

$$W_\chi(\chi) = \frac{1}{\gamma\sqrt{2\pi}} exp\left(-\frac{\chi^2}{2\gamma^2}\right), \tag{3}$$

where γ is the mean value of χ in the x direction and defined by: $\gamma = \sigma/L$ [33,46], L is the correlation length and characterizes the lateral variation of the height. To further estimate the transmission coefficient $\alpha_{1\rightarrow2,j}(\theta,\omega)$ in Eq. (1) by using the Kirchhoff approximation, the distribution of the inclination angle φ is also required. According to the relationship between continuous random variable χ and φ: $\chi = tan\varphi$, we can derive the probability function of φ:

$$W_\varphi(\varphi) = \frac{1}{\gamma\sqrt{2\pi}\cos^2\varphi} exp\left(-\frac{\tan^2\varphi}{2\gamma^2}\right). \tag{4}$$

2.2. Elastic wave model

Based on the theory of elasticity [40], we can determine the portion of incident energy transmitted through the tangent plane or the smooth interface by imposing boundary conditions. In our previous work [47], we presented an EWM for estimating the TBC across the ideal smooth interface. Different from traditional TBC models [5], the EWM estimates the transmission coefficient based on rigorous interfacial displacement and stress continuity conditions. However, this model cannot describe the effect of interfacial roughness due to the specular scattering assumption. By using the above elastic Kirchhoff approximation, we can solve this problem and extend the model to different rough interfaces. Under the Kirchhoff approximation, when a P, SV, or SH plane wave is incident at a specular point, the specular reflection and transmission occur at the tangent plane (Fig. 2).

Considering the mode conversion, the incident, reflected, and transmitted waves need to satisfy four (P and SV waves) or two (SH wave) interfacial displacement and stress continuity conditions. The properties of elastic wave propagated in isotropic solid 1 and solid 2 are determined by the Lamé coefficients (λ_1, μ_1 and λ_2, μ_2), as well as the density of materials (ρ_1 and ρ_2). According to these boundary conditions, we can calculate the amplitude ratios of the generated wave to the incident wave A_n/A_0. The derivation of the stress and displacement continuity equations is given elsewhere [40], the continuity equations for incident P, SV, and SH waves here are written in matrix notation:

$$P : \begin{bmatrix} -\sin\theta_1 & -\cos\theta_2 & \sin\theta_3 & -\cos\theta_4 \\ \cos\theta_1 & -\sin\theta_2 & \cos\theta_3 & \sin\theta_4 \\ \sin2\theta_1 & \frac{v_L}{v_T}\cos2\theta_2 & \frac{\mu^B v_L}{\mu v_L^B}\sin2\theta_3 & -\frac{\mu^B v_L}{\mu v_T^B}\cos2\theta_4 \\ -\frac{v_L^2}{v_T^2}\cos2\theta_2 & \frac{v_L}{v_T}\sin2\theta_2 & \frac{\mu^B v_L v_L^B}{\mu\left(v_T^B\right)^2}\cos2\theta_4 & \frac{\mu^B v_L}{\mu v_T^B}\sin2\theta_4 \end{bmatrix}\begin{bmatrix} A_1/A_0 \\ A_2/A_0 \\ A_3/A_0 \\ A_4/A_0 \end{bmatrix}$$

$$= \begin{bmatrix} \sin\theta_0 \\ \cos\theta_0 \\ \sin 2\theta_0 \\ \frac{v_L^2}{v_T^2}\cos 2\theta_2 \end{bmatrix}, \qquad (5)$$

$$SV : \begin{bmatrix} -\sin\theta_1 & -\cos\theta_2 & \sin\theta_3 & -\cos\theta_4 \\ \cos\theta_1 & -\sin\theta_2 & \cos\theta_3 & \sin\theta_4 \\ \frac{v_T}{v_L}\sin 2\theta_1 & \cos 2\theta_2 & \frac{\mu^B v_T}{\mu v_L^B}\sin 2\theta_3 & -\frac{\mu^B v_T}{\mu v_T^B}\cos 2\theta_4 \\ -\frac{(\lambda+2\mu\cos^2\theta_1)v_T}{\mu v_L} & \sin 2\theta_2 & \frac{(\lambda^B+2\mu^B\cos^2\theta_3)v_T}{\mu v_L^B} & \frac{\mu^B v_T}{\mu v_T^B}\sin 2\theta_4 \end{bmatrix} \begin{bmatrix} A_1/A_0 \\ A_2/A_0 \\ A_3/A_0 \\ A_4/A_0 \end{bmatrix}$$

$$= \begin{bmatrix} -\cos\theta_0 \\ \sin\theta_0 \\ -\cos 2\theta_0 \\ \sin 2\theta_0 \end{bmatrix}, \qquad (6)$$

$$SH : \begin{bmatrix} 1 & -1 \\ \cos\theta_0 & \frac{v_T\mu^B}{v_T^B\mu}\cos\theta_4 \end{bmatrix} \begin{bmatrix} A_2/A_0 \\ A_4/A_0 \end{bmatrix} = \begin{bmatrix} -1 \\ \cos\theta_0 \end{bmatrix}, \qquad (7)$$

where v_L, v_T and v_L^B, v_T^B are the velocities of longitudinal and transverse waves in solid 1 and solid 2, respectively. The angles of generated waves θ_n satisfy the Snell's law: $v_0 \sin\theta_n = v_n \sin\theta_0$. Note that θ_0 is the actual angle of incidence on the tangent plane. Using the relations $v_L^2 = (\lambda+2\mu)/\rho$ and $v_T^2 = \mu/\rho$, the Lamé elastic constants can be expressed in terms of the density and displacement velocities. By introducing material parameters of two solids into Eqs. (5)–(7), the amplitude ratios A_n/A_0, which depend on the angle of incidence θ_0, can be numerically determined.

The transmission coefficient in Eq. (1) is the total energy transmitted to solid 2 through the interface: $\alpha_{1\to 2,P\ or\ SV} = E_3/E_0 + E_4/E_0$ and $\alpha_{1\to 2,SH} = E_4/E_0$, where $E_n = \eta_n \Delta S_n$ is the average energy transmission of the corresponding wave [denoted as (n) in Fig. 2], η_n is the time-average power per unit area and ΔS_n is the cross-sectional area of the beam. The average energy transmissions per unit area for longitudinal and transverse waves are generally determined by:

$$\eta_{LA} = \frac{1}{2}\rho v_{LA}\omega^2 A^2, \qquad (8)$$

$$\eta_{TA} = \frac{1}{2}\rho v_{TA}\omega^2 A^2. \qquad (9)$$

The relation between the cross-sectional area of waves is represented by $\Delta S_n \cos\theta_0 = \Delta S_0 \cos\theta_n$, and the transmission coefficients $\alpha_{1\to 2,j}(\theta_0)$ of P, SV, and SH waves are expressed as:

$$\alpha_{1\to 2,P}(\theta_0) = \left(\frac{A_3}{A_0}(\theta_0)\right)^2 \frac{\rho^B v_L^B \cos\theta_3}{\rho v_L \cos\theta_0} + \left(\frac{A_4}{A_0}(\theta_0)\right)^2 \frac{\rho^B v_T^B \cos\theta_4}{\rho v_L \cos\theta_0}, \qquad (10)$$

$$\alpha_{1\to 2,SV}(\theta_0) = \left(\frac{A_3}{A_0}(\theta_0)\right)^2 \frac{\rho^B v_L^B \cos\theta_3}{\rho v_T \cos\theta_0} + \left(\frac{A_4}{A_0}(\theta_0)\right)^2 \frac{\rho^B v_T^B \cos\theta_4}{\rho v_T \cos\theta_0}, \qquad (11)$$

$$\alpha_{1\to 2,SH}(\theta_0) = \left(\frac{A_4}{A_0}(\theta_0)\right)^2 \frac{\rho^B v_T^B \cos\theta_4}{\rho v_T \cos\theta_0}, \qquad (12)$$

where the amplitude ratios A_n/A_0 are computed by Eqs. (5)–(7). And the transmission calculations [Eqs. (10)–(12)] are applicable for the smooth interface and tangent planes of rough interface as they specularly scatter elastic waves. Note that the AMM also assumes that phonons are specularly scattered at the interface, while it uses a simplification that the transmission coefficient $\alpha_{1\to 2,j}(\theta_0)$ is determined by the acoustic impedances of two solids [3,48]:

$$\alpha_{1\to 2,j}(\theta_0) = \frac{4 z_j z_j^B \cos\theta_0 \cos\theta^B}{\left(z_j \cos\theta^B + z_j^B \cos\theta_0\right)^2}, \qquad (13)$$

where, $j = LA$ and TA, $z_j = \rho v_j$ and $z_j^B = \rho^B v_j^B$ are the acoustic impedances of solid 1 and solid 2, respectively, where v_j^B is determined by Snell's law: $v_j^B \sin\theta_0 = v_j \sin\theta^B$. The main difference from EWM is

that AMM neglects the mode conversion between pressure wave (P) and shear wave (S) and only considers the P–P and S–S transmissions. The contribution of two polarized transmitted waves to the transmission coefficient should be considered due to the coupling of P and SV waves [Eqs. (10)–(12)]. Meanwhile, this will also affect the cut-off frequency of the transmission process [Eq. (1)].

2.3. Phonon dispersion relations

To fully describe the frequency-dependent characteristics of phonons that are important for both acoustics and heat transfer issues, it is necessary to consider lattice vibrational properties of materials. At low temperatures ($T < 20$ K), the phonon (or wave) dispersion relations $\omega(k)$ can be simplified into a linear by Debye approximation. However, THz phonons dominate the heat transfer at high temperatures and Debye linear approximation cannot accurately describe the vibration characteristics of them, as shown in Fig. 3. It has been demonstrated that the AMM and DMM with Debye linear dispersions (v_j is independent of ω) well predict the low-temperature TBC [2], while they overestimate the TBC at high temperatures [3,47]. Therefore, we incorporate the nonlinear phonon dispersions $\omega(k)$ in EWM.

We take silicon and aluminum as example materials, as they are typical media of interest [51–54]. For an Al/Si interface, we specify the real dispersion relations of the Al film and the Si substrate by fitting polynomials to the measured curves of acoustic branches [55, 56]. Since the group velocities of the optical dispersion branches of phonons are small, their contribution to the heat transfer is generally negligible [54]. We assume that the crystals are isotropic and utilize the measured acoustic dispersions along the [100] crystal orientation. Fig. 3 shows the fitting of one-dimensional phonon dispersions in the [100] direction using polynomials: $\omega(k) = a_4 k^4 + a_3 k^3 + a_2 k^2 + a_1 k + a_0$ (for TA), and $\omega(k) = b_3 k^3 + b_2 k^2 + b_1 k + b_0$ (for LA). The group velocities $v_{g,j}(\omega) = \partial\omega/\partial k$ and phase velocities $v_{p,j}(\omega) = \omega/k$ change from constants (Debye approximation) to frequency-dependent values. In addition, the specular reflection and transmission of the interface do not change the frequency of phonons or elastic waves [40,54]. And we can introduce the frequency-dependent velocities of Al and Si from dispersions into the sets of continuity equations (5)–(7), and obtain the frequency-dependent interfacial boundary conditions that can illustrate the vibration spectra of two solids. By solving these equations, we determine the amplitude ratios of generated waves to the incident wave $A_n/A_0(\theta_0,\omega)$. In this case, the transmission coefficients calculated by Eqs. (10)–(12) depend on the mode, angle of incidence, and frequency of phonons. And the transmission coefficients $\alpha_{1\to 2,j}(\theta_0,\omega)$ of P, SV, and SH waves that are specularly scattered on the tangent plane (Fig. 2) can be rewritten as:

$$\alpha_{1\to 2,P}(\theta_0,\omega) = \left(\frac{A_3}{A_0}(\theta_0,\omega)\right)^2 \frac{\rho^B v_L^B(\omega)\cos\theta_3}{\rho v_L(\omega)\cos\theta_0} + \left(\frac{A_4}{A_0}(\theta_0,\omega)\right)^2 \frac{\rho^B v_T^B(\omega)\cos\theta_4}{\rho v_L(\omega)\cos\theta_0}, \qquad (14)$$

$$\alpha_{1\to 2,SV}(\theta_0,\omega) = \left(\frac{A_3}{A_0}(\theta_0,\omega)\right)^2 \frac{\rho^B v_L^B(\omega)\cos\theta_3}{\rho v_T(\omega)\cos\theta_0} + \left(\frac{A_4}{A_0}(\theta_0,\omega)\right)^2 \frac{\rho^B v_T^B(\omega)\cos\theta_4}{\rho v_T(\omega)\cos\theta_0}, \qquad (15)$$

$$\alpha_{1\to 2,SH}(\theta_0,\omega) = \left(\frac{A_4}{A_0}(\theta_0,\omega)\right)^2 \frac{\rho^B v_T^B(\omega)\cos\theta_4}{\rho v_T(\omega)\cos\theta_0}. \qquad (16)$$

Note that, the cut-off frequency $\omega_c = 4.486$ THz (Fig. 3), which determines the upper limit of the integral in Eq. (1), is defined as the minimum of four maximum frequencies $\omega_{max,j}$ at the edge of the first Brillouin zone of Al and Si. Other high-frequency incident waves from solid 1 lacking a corresponding state of transmitted waves in solid 2 cause the breaking of interfacial boundary conditions [54]. These
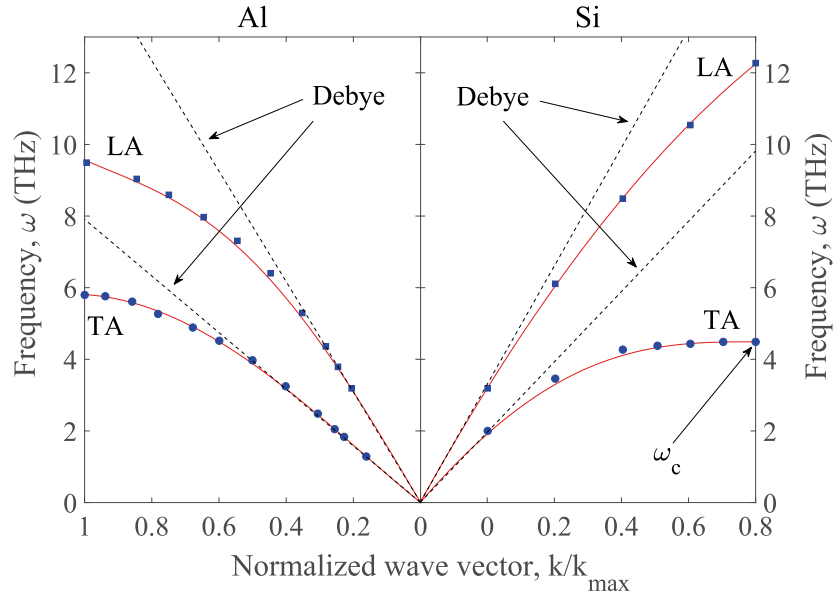
Fig. 3. The phonon dispersions of aluminum (left) and silicon (right) along the [100] direction. The measured longitudinal acoustic (LA) and transverse acoustic (TA) dispersion curves are represented by squares and circles, respectively [49,50]. The solid line is the polynomial fitting result of the real dispersions in this work. The dashed lines are the linear dispersion relations using Debye approximation.

incident waves cannot be transmitted and will be totally reflected [19]. This is similar to the total internal reflection phenomenon that occurs when the angle of incidence is greater than the critical angle $\theta_0 > \theta_c$.

Moreover, Fig. 2 has shown other frequency limitations caused by the characteristic length in this problem. In the frequency integration interval of Eq. (1), $0 < \omega < \omega_c$, it is necessary to compare the wavelength of phonon waves $\lambda = 1/k = v_p/\omega$ with the lateral parameters of interface roughness L [45]. For phonons with wavelength $\lambda > L$, the rough interface can be regarded as a smooth interface, and simple specular reflection and transmission process occurs (Fig. 2) [33]. On the contrary, when the wavelength λ is comparable with or smaller than the correlation length L, the incident waves are scattered by the rough interface, which is determined by the Kirchhoff approximation. It is worth noting that according to the cumulative TBC, $\int_0^\omega h_K(\omega)\,d\omega$ (the superposition of the contribution of phonons with frequencies from 0 to a certain value ω) [57], thermal transport at Si-substrate interface is carried by phonons with sub-THz and THz frequencies (or wavelength $\lambda \le 10$ nm). The thermal transport contribution of phonons with wavelengths $\lambda > 10$ nm is less than 1% and could be ignored. These two cases need to be taken into account when evaluating the frequency integral of Eq. (1) in the next section.

2.4. Effective transmission coefficient

In Eqs. (14)–(16) the angle θ_0 is the actual angle of incidence at a specular point (Fig. 2), while in the Landauer formula [Eq. (1)], the transmission coefficient $\alpha_{1\to2,j}(\theta,\omega)$ is dependent on the angle θ, which is defined as the angle of incidence relative to the mean plane $z = 0$ of the random rough interface. We need to estimate the transmission coefficient $\alpha_{1\to2,j}(\theta,\omega)$ of rough interface based upon Eqs. (14)–(16). By introducing the relation of angles $\theta_0 = \theta_0(\varphi,\varphi)$ from interface geometry (described in detail below) into Eqs. (14)–(16), we can determine the "specular" transmission coefficient $\alpha_{1\to2,j}(\theta,\varphi,\omega)$ at each point of the rough interface. This specular transmission coefficient $\alpha_{1\to2,j}(\theta,\varphi,\omega)$ is a function of the continuous random variable φ. Based on the distribution function $W_\varphi(\varphi)$, we calculate the expected value of $\alpha_{1\to2,j}(\theta,\varphi,\omega)$ for the entire rough interface and regard it as the effective transmission coefficient $\alpha_{1\to2,j,eff}(\theta,\omega)$. In other words, the dependence of specular transmission coefficient $\alpha_{1\to2,j}(\theta,\varphi,\omega)$ on the angle of inclination φ is numerically eliminated. And this quantitative calculation is determined

by the roughness of interface. Therefore, an ensemble averaging is performed numerically to obtain the expected transmission coefficient of the rough interface:

$$\alpha_{1\to2,j,eff}(\theta,\omega) = \int_{\varphi_{min}}^{\varphi_{max}} \alpha_{1\to2,j}(\theta,\varphi,\omega)\, W_\varphi(\varphi)\, d\varphi, \tag{17}$$

where, the probability density function $W_\varphi(\varphi)$ of φ is given by Eq. (4). It is seen from Eq. (17) that when $\varphi = 0$, $\alpha_{1\to2,j,eff}(\theta,\omega) = \alpha_{1\to2,j}(\theta,\omega)$, which represents a completely specular wave scattering at the smooth interface. When the tangent plane of a certain point is parallel to the mean plane $z = 0$, its angle of inclination φ is regarded as zero. As a result, Eq. (17) is valid for both the smooth interface and the tangent plane. By substituting $\theta_0 = \theta$ into Eqs. (14)–(16), we can directly compute the transmission coefficient at the smooth interface.

In addition, the range of the Gaussian-distributed interface gradient is infinity. In order to numerically calculate Eq. (17), we need to determine the integral range of the slope angle (φ_{min} and φ_{max}). As is well known, almost all values (99.7%) of Gaussian distribution are within three standard deviations of the mean $[-3\sigma, 3\sigma]$, which is the so-called three-sigma rule in statistics [58]. The slope angle φ is not Gaussian distributed and in Fig. 4(a) we plot the probability distribution of φ calculated by Eq. (4). For the roughness $\sigma = 1, 5$, and 10 nm and the correlation length $L = 15$ nm considered in this work, it is clear that nearly all values lie within the range of $-\pi/2 \le \varphi \le \pi/2$. Therefore, we take the values $\varphi_{min} = -\pi/2$ and $\varphi_{max} = \pi/2$ in numerical calculations, and the deviation could be ignored. For some rough interfaces with large gradient and change rate of slope angle, additional consideration of the numerical integration range Fig. 4(a) is required, while this has little impact on practical problems of nanoscale interfacial heat transfer.

Further, we determine the actual incident angle θ_0 of a wave in arbitrary direction θ at a certain point with slope angle φ. This angular relationship can be denoted as $\theta_0 = \theta_0(\theta,\varphi)$. In the TBC model [Eq. (1)], the angle of incidence θ varies from 0 to $\pi/2$, and the range of φ has been stated above: $-\pi/2 \le \varphi \le \pi/2$. Fig. 4(c) shows three cases of the wave incident in different directions at a certain point on the rough interface. We emphasize that as φ increases and $\varphi \ge \pi/2 - \theta$, it is obvious that the incident wave will "miss" the point, and no energy is transmitted through this point [33]. This is equivalent to the case of wave glancing on the interface, $\theta_0 = \pi/2$, and this point belongs to the
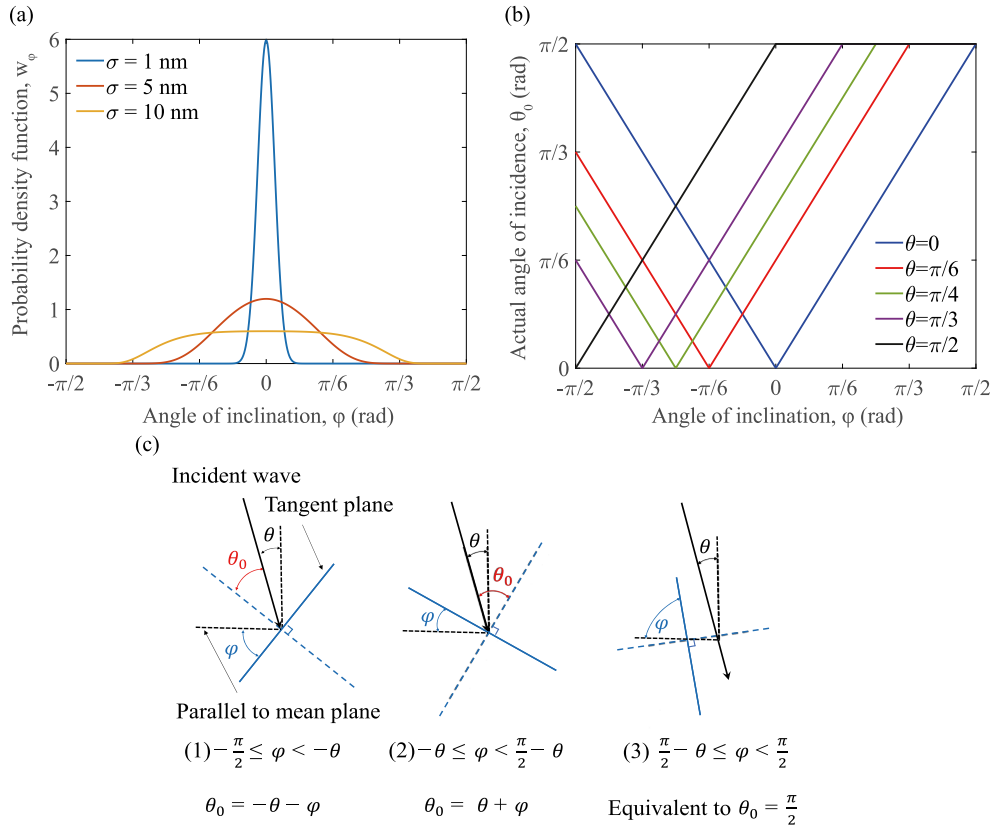
Fig. 4. (a) Probability distribution of the slope angle φ at the rough interface, when $\sigma = 1, 5,$ and 10 nm and $L = 15$ nm. (b) Calculated actual angle of incidence θ_0 as a function of the slope angle φ: $\theta_0 = \theta_0(\theta, \varphi)$, when $\theta = 0, \pi/6, \pi/4, \pi/3,$ and $\pi/2$, respectively. (c) Schematic of three cases of actual incident angle θ_0 on the tangent plane, the ranges of θ and φ are $0 \leq \theta \leq \pi/2$ and $-\pi/2 \leq \varphi \leq \pi/2$, respectively.

"shadow area", as shown in Fig. 2. In Fig. 4(b) we plot the curves of $\theta_0 = \theta_0(\theta, \varphi)$ by taking $\theta = 0, \pi/6, \pi/3, \pi/4,$ and $\pi/2$ as examples. In numerical calculations, we integrate θ from 0 to $\pi/2$. By introducing $\theta_0 = \theta_0(\theta, \varphi)$ into Eqs. (14)–(16) and using Eq. (17), we determine the effective transmission coefficient $\alpha_{1 \to 2, j, eff}(\theta, \omega)$ of the random rough interface. Ultimately, the TBC is calculated by substituting the effective transmission coefficient $\alpha_{1 \to 2, j, eff}(\theta, \omega)$ into Eq. (1).

3. Results and discussion

Now we turn into a TBC calculation to examine applicability of the theoretical model. This section contains numerical results and discussion of the transmission spectra, amplitude and energy ratios of generated waves to the incident wave, and the TBC at rough Al/SiO$_2$/Si and Au/SiO$_2$/Si interfaces.

3.1. Angle- and frequency-dependent transmission spectrum

In order to rigorously understand the thermal transport of phonons at the interface, an accurate description of the phonon scattering is necessary. We calculate the effective transmission coefficient $\alpha_{1 \to 2, j, eff}(\theta, \omega)$ by Eq. (17) at perfect smooth ($\sigma = 0$) and rough ($\sigma = 1, 5,$ and 10 nm) Al/Si interfaces, respectively. In these calculations we use the Gaussian-distributed rough interface with correlation length $L = 15$ nm. For the interface in heat flow equilibrium, the TBC calculated from the solid on either side should be the same [24]. In order to avoid considering the total reflection at the interface and simplify the calculation, we regard Si as solid 1, which has higher velocities than Al (solid 2). The contour plots of angle- and frequency-dependent transmission spectra of P, SV and SH modes are shown in Fig. 5.

Clearly, Fig. 5 indicates that both the phonon frequency and angle of incidence significantly influence the transmission coefficient at sample

interfaces. The transmissions of incident SV and SH waves have a clear drop when their frequency is higher than 3 THz, while the trend of P wave in the entire frequency range is flat. This phenomenon is attributed to the low velocities for transverse polarizations $v_{g, TA}(\omega)$ at the edge of the first Brillouin zone, as shown in Fig. 3. In the THz frequency regime, the contribution of low-frequency phonons is generally higher than that of high-frequency phonons. These results suggest that the phononic mismatch between two materials (the cut-off frequency and the frequency-dependent velocities determined by the dispersions of solids 1 and 2) significantly impacts the spectral contribution to interfacial thermal transport. While the phonon flux determines the magnitude of TBC at a certain interface, the transmission coefficient $\alpha_{1 \to 2, j}(\theta, \omega)$ directly affects the phonon frequencies at which energy is transferred across the interface.

On the other hand, the model provides a description of the oblique incidence of phonons. In Fig. 5, when the angle of incidence θ is small and close to normal incidence, the phonons have nearly 100% transmission. And the transmission coefficient decreases with increasing θ. As the angle of incidence θ approaches the maximum value $\pi/2$, the propagation directions of phonons are nearly parallel to the interface and the transmission coefficient decreases to zero, which is similar to the grazing incidence of the wave. These results highlight the importance of angle dependence of the transmission coefficient, which is ignored in commonly used DMM that assumes the diffuse scattering of phonons and calculates the transmission coefficient by the energy conservation of the scattering process [24,57]. That is, the transmission coefficients of all phonons with various incident angles are the same. In addition, the interface specularity parameter $p = \exp\left(-16\pi^2\sigma^2/\lambda^2\right)$ represents the fraction of phonons experiencing specular scattering at the interface [59]. This parameter is used in TBC calculations [9,27,60] to estimate the transmission coefficients of rough interfaces by assuming that phonons are partially specularly and partially diffusely scattered
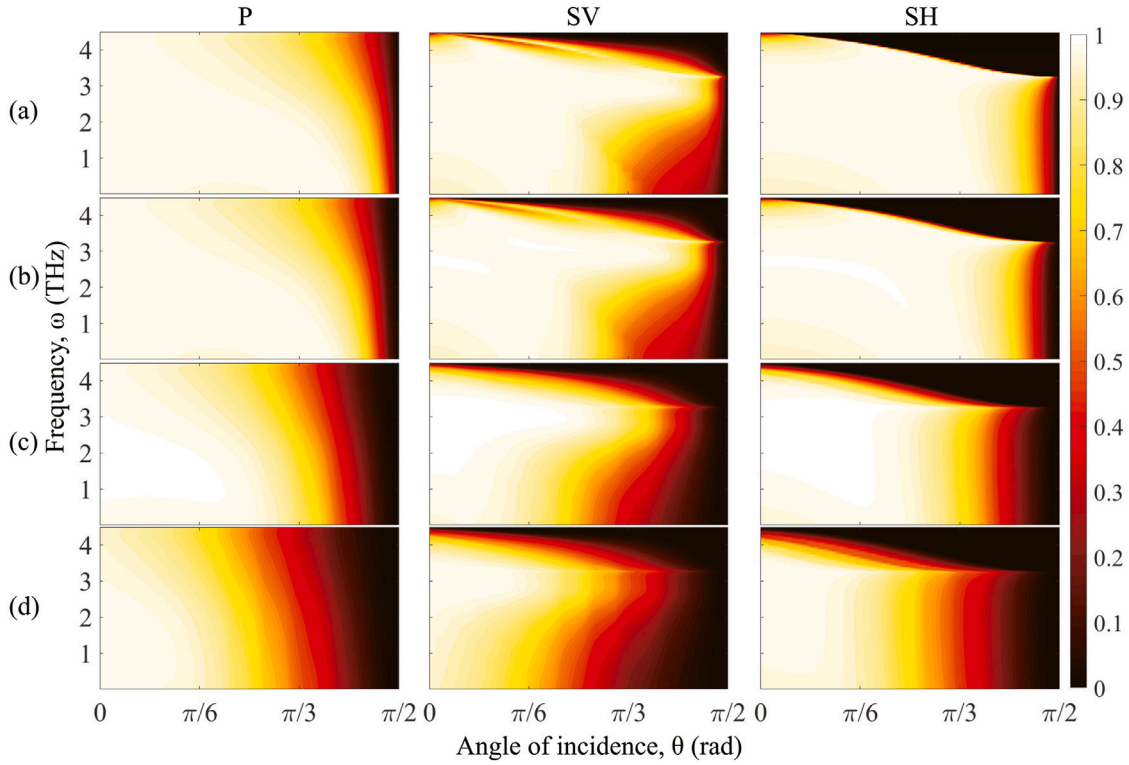
Fig. 5. Contour plots of transmission coefficient $\alpha_{1\to2,j}(\theta,\omega)$ as a function of angle of incidence and frequency for P, SV, and SH waves incident at different Al/Si interfaces: (a) ideal smooth, (b) RMS roughness $\sigma = 1$ nm, (c) $\sigma = 5$ nm and (d) $\sigma = 10$ nm. The values of transmission coefficients (0 to 1) are indicated on the right scale.

at the interface. Since it assumes normal incidence and ignores the mode conversion, the specularity parameter has been found to differ from the predictions of boundary perturbation and Green's function approaches [61].

The EWM also gives insights on the variation of phonon–interface interaction with interfacial roughness. As shown in Fig. 5, the overall trend of transmission coefficient decreases with increasing roughness, especially for phonons near normal incidence. While it is worth noting that when the RMS roughness σ is less than 1 nm, transmission coefficients of the rough and smooth interfaces for all three polarizations should be very close. This indicates that in the TBC calculation, the EWM of the perfect interface ignoring the interfacial irregularities is also applicable to the prediction of the atomically smooth interface (the magnitude of σ is sub-nanometers, 10^{-10} m). In addition, the Al/Si transmission coefficient profile versus the phonon frequency (or wavelength) indicates that as the interface gets rougher, phonons with frequencies $\omega < 4$ THz are more likely to be reflected. This intuitive image is consistent with the experimental conclusion [62].

3.2. Wave characteristics of phonons

To illustrate the magnitude of mode conversion and the angle-dependent scattering of phonons or waves, we compute the amplitude and energy ratios of generated waves to the incident wave of the Al/Si system. Instead of frequency-dependent velocities calculated by nonlinear dispersions (Fig. 3), we use constant longitudinal and transverse wave velocities of 8970 m/s, 5332 m/s for Si and 6240 m/s, 3040 m/s for Al [5] to compute the continuity equations (5)–(7). And the amplitude ratios $A_n/A_0(\theta_0,\varphi)$ of each point on the rough profile are obtained. Analogous to Eq. (17), we can determine the ensemble average of amplitude ratios at the rough interface by $A_n/A_0(\theta) = \int_{\varphi_{min}}^{\varphi_{max}} A_n/A_0(\theta,\varphi) W_\varphi(\varphi) d\varphi$. Using Eqs. (8) and (9), the expected energy ratios of reflected and transmitted waves are calculated by $E_n/E_0(\theta) = \int_{\varphi_{min}}^{\varphi_{max}} E_n/E_0(\theta,\varphi) W_\varphi(\varphi) d\varphi$. Fig. 6 shows the quantitative influence of interfacial roughness on the energy

distribution of generated waves. The value of transmission coefficient is the summation of energy ratios of transmitted P wave and transmitted SV wave: $\alpha = E_3/E_0 + E_4/E_0$.

In Fig. 6, the transmission coefficient $\alpha(\theta)$ is close to 1 when the wave is near normal incidence (small θ). As the RMS roughness σ increases, $\alpha(\theta)$ decreases rapidly within the range of θ from $\pi/4$ to $\pi/2$. The results indicate that interfacial irregularity reduces the proportion of transmitted waves and enhances the reflection of the incident wave, especially for the reflected P–P mode (E_1/E_0 curves in Fig. 6). It can be seen that the variation of transmission coefficient $\alpha(\theta)$ with incident angle and roughness for P wave is consistent with Fig. 5. The roughness has a greater influence on the scattering angles $\cos\theta_n/\cos\theta_0$ in Eqs. (10)–(12) than that on amplitude of waves. As a consequence, the increase of σ has a weak effect on the trend and magnitude of A_n/A_0 curves, while the curves of energy ratios E_n/E_0 has been significantly changed. Waves obliquely incident on nanostructures with rough interfaces have a lower transmission coefficient than normally incident waves, and dissipate faster as the transmission distance increases.

3.3. Thermal boundary conductance at rough interfaces

To quantify and analyze the effect of roughness on interfacial heat transfer, we compute the TBC as a function of temperature for smooth and rough Al/Si interfaces by the EWM. In Fig. 7, the theoretical results of TBC (solid lines) are compared with the measurement (circles) [63]. In the experiment the interfacial roughness is not characterized, while high purity natural Si wafers is used and the natural oxide of the wafer is removed by HF etching before Al evaporation [63]. The Al/Si interface measured in this work can be regarded as atomically or nominally smooth [15]. The dashed lines in Fig. 7 represent the TBC values predicted by AMM and DMM calculations. Instead of the Debye approximation, here we use nonlinear dispersion relations in the AMM and DMM, which have higher accuracy at high temperatures [24].

The ideal EWM for smooth interface [Eqs. (14)–(16)] agrees well with the measurement within 5% over a wide temperature range
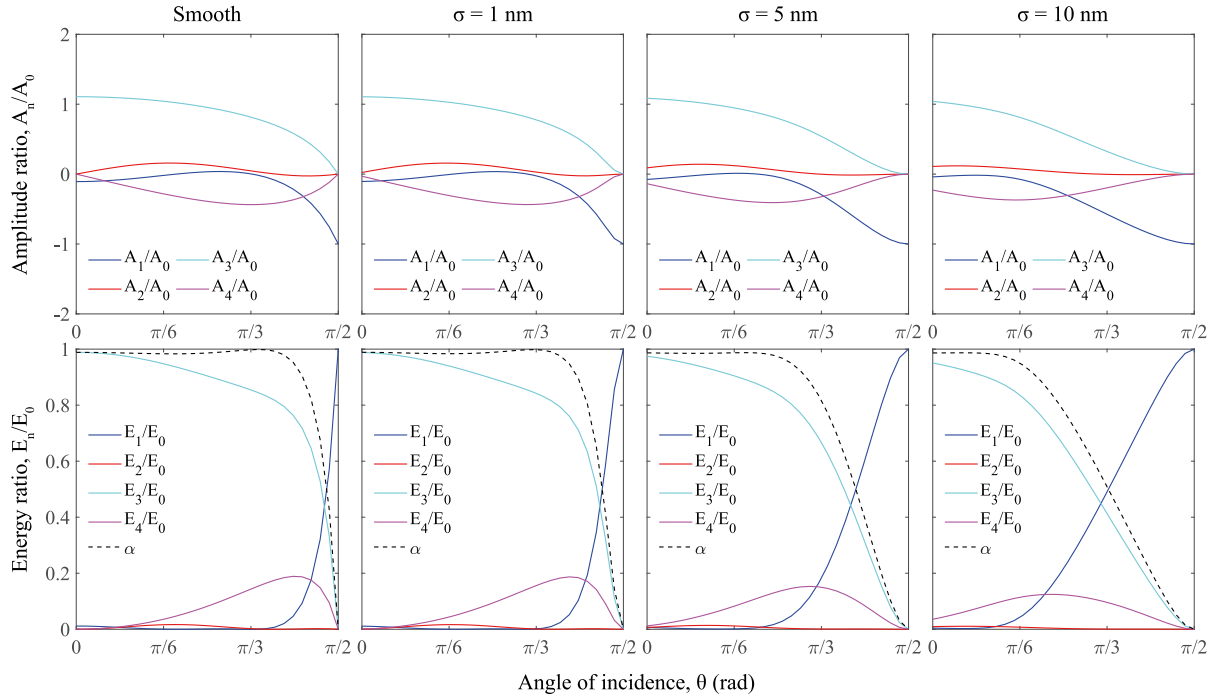
Fig. 6. Calculated amplitude and energy ratios of generated waves as a function of angle of incidence for the P wave incident at different Al/Si interfaces. The transmission coefficient α is the summation of energy ratios of transmitted P wave (3) and transmitted SV wave (4).
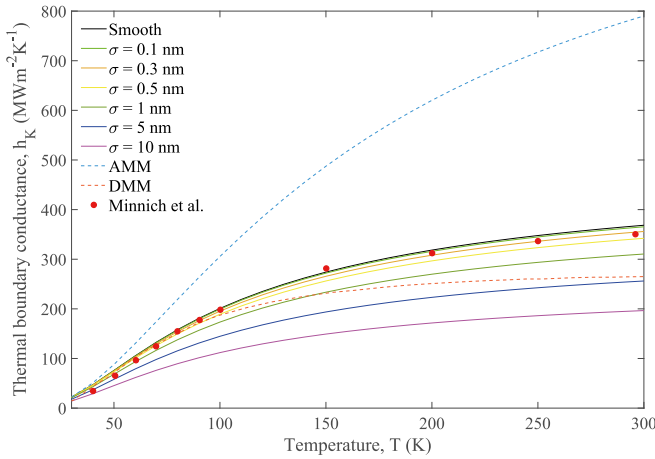

Fig. 7. Calculated TBC by the EWM as a function of temperature at smooth and rough Al/Si interfaces (solid lines). Our results are compared with the measurement at the atomically smooth interface (circles) [63] and the theoretical predictions of AMM and DMM (dashed lines).

(30–300 K). At temperatures T > 100 K, the EWM achieves better predictions compared with the AMM and DMM. Note that for higher temperatures (T > 400 K), the influence of the inelastic process needs to be considered [64], and Eq. (1) may require estimating the equivalent equilibrium temperature for highly-matched interfaces [65]. For the EWM-predicted TBC at rough interfaces, results in Fig. 7 show that as σ less than 0.5 nm, the interfacial roughness has small impact on the TBC and the curves are close to the smooth interface. This explains why the ideal EWM without consideration of interfacial irregularities agrees well with the TBC measurement of the atomically smooth interface. The overestimation of phonon scattering and deviation from the measured result of DMM at T > 100 K are due to its assumption of completely diffuse scattering. However, in Fig. 7 the DMM agrees well with the EWM predictions of interfaces with RMS roughness from 1 nm to 5 nm,

indicating that the DMM can give a good prediction for the interface with a certain roughness. In addition, as mentioned in Section 2.2, the AMM neglects the mode conversion and overpredicts the transmission of waves, while it can well predict the TBC at low temperatures (T < 30 K) [2]. More importantly, the AMM and DMM are currently unable to evaluate the impact of roughness on TBC. Our quantitative analysis verifies the above general conclusions about the existing theoretical models [24].

It is worth noting that at the Al/Si interface in Fig. 7, the room-temperature TBC decreases monotonically about 47% from 370 MWm^{-2}K^{-1} for smooth interface to 197 MWm^{-2}K^{-1} for rough interface with $\sigma = 10$ nm. For T = 40 K, and within the same σ rising range, the TBC decreases from 47 MWm^{-2}K^{-1} to 29 MWm^{-2}K^{-1} with only 38% change. Compared with the smooth interface, the rise of the TBC curve of rough interface is relatively flat. We conclude that as domain carriers at high temperatures, short-wavelength phonons are more significantly scattered by rough interfaces.

To further validate the model, we compute the room-temperature TBC as a function of interfacial roughness and compare it with the experimental studies [13–15]. For comparison, another factor that needs to be considered is the thermal resistance R_{oxide}, which is caused by the native oxide layer (SiO$_2$) on the Si-substrate surface. This thermal resistance is generally approximated as the native-oxide-layer thickness divided by its thermal conductivity [15,66], and the thermal conductance of this layer can be expressed by:

$$h_{oxide} = R_{oxide}^{-1} = \frac{\kappa_{oxide}}{d_{oxide}}, \tag{18}$$

where, the native-oxide-layer thickness d_{oxide} on the sample surface is approximately 2 nm measured by transmission electron microscopy [13–15], and its thermal conductivity κ_{oxide} is commonly assumed as the thermal conductivity of the bulk material. Considering the influence of size effect, here the thermal conductivity κ_{oxide} is given by the measured value of SiO$_2$ thin film and $\kappa_{oxide} = 0.952$ Wm^{-2}K^{-1} [67]. The effective TBC at the interface with a native oxide layer is given by

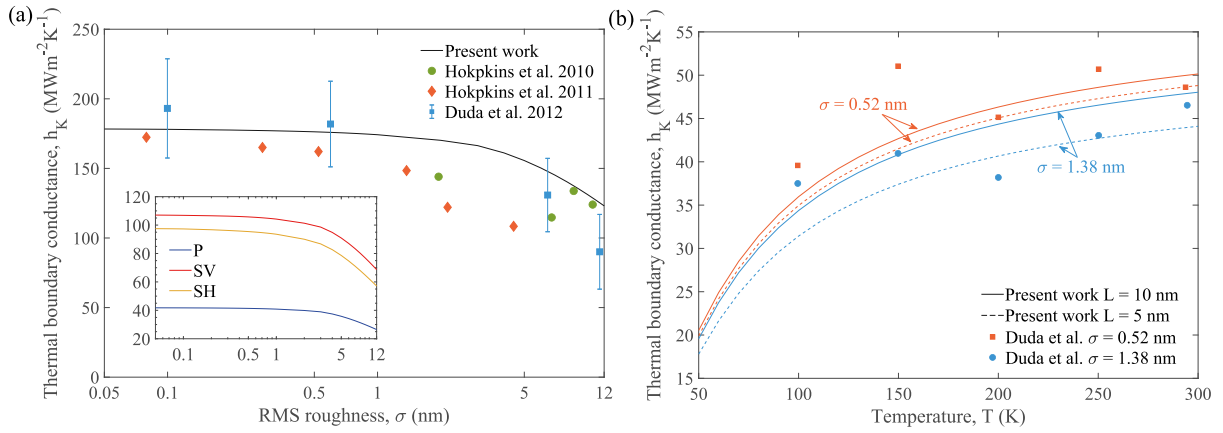$$h_K = \left(h_{K,EWM}^{-1} + h_{oxide}^{-1} \right)^{-1}. \tag{19}$$

Fig. 8. (a) Calculated and measured room-temperature TBC of rough Al/SiO$_2$/Si interfaces as a function of RMS roughness σ. In experiments, the rough surfaces of Si substrate are prepared by chemical etching (diamonds and squares) [13,15] and quantum dot (circles) [14], respectively. The inset shows the contribution of P, SV, and SH waves to the total TBC. (b) Calculated and measured TBC [68] of Au/SiO$_2$/Si interfaces with RMS roughness σ = 0.52 nm and 1.38 nm. The solid and dashed lines represent the theoretical results with the correlation length L = 10 nm and 5 nm, respectively.

The room-temperature TBC of the rough Al/SiO$_2$/Si interface is calculated by Eq. (19) for RMS roughness σ from 0 to 12 nm and correlation length L = 15 nm. The maximum value of σ/L is 0.8, which is within the reasonable range of σ/L in the experiment [46]. Fig. 8(a) shows the comparison between the theoretical and measured TBC values. In experiments, the rough Al/Si interfaces are prepared by different processing methods [13–15]. The plot shows the quantitative agreement between theory and measurement within the uncertainty range. From the work [67], the measured room-temperature thermal conductivities of SiO$_2$ layers with thickness 6.5 nm, 11.8 nm, and 25 nm are 0.952 Wm^{-1}K^{-1}, 1.049 Wm^{-1}K^{-1} and 1.265 Wm^{-1}K^{-1}, respectively. Although the thermal conductivity of thick layers of thermally grown SiO$_2$ with thickness 25 nm are essentially identical with the bulk SiO$_2$ (1.289 Wm^{-1}K^{-1}). The thermal conductivity κ_{oxide} = 0.952 Wm^{-1}K^{-1} used in Eq. (18) still overestimate the value of the SiO$_2$ interlayer with a thickness of 2 nm, which may lead to an increase in the predicted value of the total TBC. The agreement between the predicted and measured TBC indicates that the EWM is a feasible model to interpret the heat transfer at the rough interface.

The inset in Fig. 8(a) shows a difference between the contributions of SV and SH waves to the TBC by using the EWM. However, in some theoretical studies it is assumed that two transverse modes of phonons have the same contribution to heat transfer [24]. The result also shows that when the RMS roughness σ is less than 1 nm, it has a weak impact on the TBC at the Al/SiO$_2$/Si interface. As the interface roughness increases further, the TBC will be significantly reduced. As the roughness rises to 12 nm, the TBC decreases approximately 30%. Furthermore, these results demonstrate the transition between two interface states based on the roughness. When the roughness is at sub-nanometers (10^{-10} m), the TBC is almost constant as a certain temperature, and its value is close to that of the corresponding smooth interface. This conclusion is consistent with the molecular dynamics simulations [23], verifying the possibility of systematically controlling the overall thermal conductivity of composite materials by changing the interfacial roughness.

For further verification, we compare the model with the TBC experimental data of Au/SiO$_2$/Si interfaces with roughness σ = 0.52 nm and 1.38 nm [68], as shown in Fig. 8(b). The thickness of SiO$_2$ layer between the Au/Si interface is 2 nm [68], and the results of EWM with correlation length L from 5 nm to 10 nm are consistent with experimental values. This indicates that the elastic process dominates the interface with nano-scale roughness, and the continuum model shows the feasibility of quantifying the roughness effect on TBC in this regime. Same as most multilayer nanostructures [69–71], the studied Al/SiO$_2$/Si and Au/SiO$_2$/Si interfaces are prepared by epitaxial

growth [14,20] or atomic layer deposition [13,68]. The high interface quality avoids the larger interface defects (e.g., porosity) [67,72], which needs to be taken into account as the characteristic size of the structure is much larger than the wavelength of the phonon wave [73].

In addition, several numerical studies attribute the difference between DMM predictions and the experiments to the electron–phonon energy transfer pathway [74,75], while recent study shows that elastic phonon transport dominates the interfacial heat transfer for various epitaxial metal/sapphire interfaces, and other mechanisms are negligible [37]. The influence of electron–phonon coupling on the heat transfer at the metal–nonmetal interface is still controversial. In this work, the presence of a SiO$_2$ intermediate layer in the samples could inhibit the effect of this electron–phonon mechanism. At higher temperatures or for highly dissimilar materials, inelastic phonon processes and other energy transport mechanisms may need to be considered [76–79]. Furthermore, the EWM based on the wave characteristics could effectively quantify the influence of interfacial roughness on coherent phonons that maintain the phase continuity in the periodic structures [69].

4. Conclusion

In summary, we present an analytical model for the TBC at rough interfaces based on the elastic wave theory. In particular, this model interprets the interfacial heat transfer of phonons by utilizing their wave nature. This approach combines a statistical description of interfacial scattering using Kirchhoff approximation with the accurate estimation of transmission coefficients based on the interface elasticity. The numerical results of transmission coefficients and TBC in a wide range of roughness confirm the validity of this framework for estimating interfacial heat transport. Compared with the traditional models, the EWM gives more in-depth physical images of phonon transmission and their wave characteristics. These considerations can provide guidance for the optimization of heat transfer in nanostructures based on the phonon wave effects. In addition, our calculations verify the transition of TBC values from a smooth interface to a nanoscale rough interface and also the influence of interlayer on thermal transport. Inserting an interlayer is also a common method to control the interfacial thermal transport. Based on the EWM, sandwich-structured composite and other multilayer periodic nanostructures can be further studied by the scattering of coherent phonons in layered media. The elastic wave or continuity theory has shown broad prospects in inspiring and guiding the design of extreme thermal conductivity materials.

Declaration of competing interest

The authors declare that they have no known competing financial interests or personal relationships that could have appeared to influence the work reported in this paper.

References

[1] Cahill DG, Ford WK, Goodson KE, Mahan GD, Majumdar A, Maris HJ, et al. Nanoscale thermal transport. J Appl Phys 2003;93(2):793–818. http://dx.doi.org/10.1063/1.1524305.

[2] Cahill DG, Braun PV, Chen G, Clarke DR, Fan S, Goodson KE, et al. Nanoscale thermal transport. II. 2003–2012. Appl Phys Rev 2014;1(1):011305. http://dx.doi.org/10.1063/1.4832615.

[3] Giri A, Hopkins PE. A review of experimental and computational advances in thermal boundary conductance and nanoscale thermal transport across solid interfaces. Adv Funct Mater 2020;30(8):1903857. http://dx.doi.org/10.1002/adfm.201903857.

[4] Moore AL, Shi L. Emerging challenges and materials for thermal management of electronics. Mater Today 2014;17(4):163–74. http://dx.doi.org/10.1016/j.mattod.2014.04.003.

[5] Swartz ET, Pohl RO. Thermal boundary resistance. Rev Modern Phys 1989;61(3):605–68. http://dx.doi.org/10.1103/RevModPhys.61.605.

[6] Losego MD, Grady ME, Sottos NR, Cahill DG, Braun PV. Effects of chemical bonding on heat transport across interfaces. Nature Mater 2012;11(6):502–6. http://dx.doi.org/10.1038/nmat3303.

[7] Zhan T, Oda K, Ma S, Tomita M, Jin Z, Takezawa H, et al. Effect of thermal boundary resistance between the interconnect metal and dielectric interlayer on temperature increase of interconnects in deeply scaled VLSI. ACS Appl Mater Interfaces 2020;12(19):22347–56. http://dx.doi.org/10.1021/acsami.0c03010.

[8] Li X, Park W, Wang Y, Chen YP, Ruan X. Reducing interfacial thermal resistance between metal and dielectric materials by a metal interlayer. J Appl Phys 2019;125(4):045302. http://dx.doi.org/10.1063/1.5079428.

[9] Duda JC, Beechem TE, Smoyer JL, Norris PM, Hopkins PE. Role of dispersion on phononic thermal boundary conductance. J Appl Phys 2010;108(7):073515. http://dx.doi.org/10.1063/1.3483943.

[10] Gotsmann B, Lantz MA. Quantized thermal transport across contacts of rough surfaces. Nature Mater 2013;12(1):59–65. http://dx.doi.org/10.1038/nmat3460.

[11] Hopkins PE. Thermal transport across solid interfaces with nanoscale imperfections: Effects of roughness, disorder, dislocations, and bonding on thermal boundary conductance. ISRN Mech Eng 2013;2013:1–19. http://dx.doi.org/10.1155/2013/682586.

[12] Smith B, Lindsay L, Kim J, Ou E, Huang R, Shi L. Phonon interaction with ripples and defects in thin layered molybdenum disulfide. Appl Phys Lett 2019;114(22):221902. http://dx.doi.org/10.1063/1.5099103.

[13] Hopkins PE, Phinney LM, Serrano JR, Beechem TE. Effects of surface roughness and oxide layer on the thermal boundary conductance at aluminum/silicon interfaces. Phys Rev B 2010;82(8):085307. http://dx.doi.org/10.1103/PhysRevB.82.085307.

[14] Hopkins PE, Duda JC, Petz CW, Floro JA. Controlling thermal conductance through quantum dot roughening at interfaces. Phys Rev B 2011;84(3):035438. http://dx.doi.org/10.1103/PhysRevB.84.035438.

[15] Duda JC, Hopkins PE. Systematically controlling kapitza conductance via chemical etching. Appl Phys Lett 2012;100(11):111602. http://dx.doi.org/10.1063/1.3695058.

[16] Mosso N, Drechsler U, Menges F, Nirmalraj P, Karg S, Riel H, et al. Heat transport through atomic contacts. Nature Nanotechnol 2017;12(5):430–3. http://dx.doi.org/10.1038/nnano.2016.302.

[17] Blank M, Weber L. Towards a coherent database of thermal boundary conductance at metal/dielectric interfaces. J Appl Phys 2019;125(9):095302. http://dx.doi.org/10.1063/1.5085176.

[18] Zhao J, Zhao R, Huo Y, Cheng W. Effects of surface roughness, temperature and pressure on interface thermal resistance of thermal interface materials. Int J Heat Mass Transfer 2019;140:705–16. http://dx.doi.org/10.1016/j.ijheatmasstransfer.2019.06.045.

[19] Ravichandran NK, Zhang H, Minnich AJ. Spectrally resolved specular reflections of thermal phonons from atomically rough surfaces. Phys Rev X 2018;8(4):041004. http://dx.doi.org/10.1103/PhysRevX.8.041004.

[20] Hopkins PE, Duda JC, Clark SP, Hains CP, Rotter TJ, Phinney LM, et al. Effect of dislocation density on thermal boundary conductance across GaSb/GaAs interfaces. Appl Phys Lett 2011;98(16). http://dx.doi.org/10.1063/1.3581041.

[21] Termentzidis K, Chantrenne P, Keblinski P. Nonequilibrium molecular dynamics simulation of the in-plane thermal conductivity of superlattices with rough interfaces. Phys Rev B 2009;79(21):214307. http://dx.doi.org/10.1103/PhysRevB.79.214307.

[22] Termentzidis K, Merabia S, Chantrenne P, Keblinski P. Cross-plane thermal conductivity of superlattices with rough interfaces using equilibrium and nonequilibrium molecular dynamics. Int J Heat Mass Transfer 2011;54(9):2014–20. http://dx.doi.org/10.1016/j.ijheatmasstransfer.2011.01.001.

[23] Merabia S, Termentzidis K. Thermal boundary conductance across rough interfaces probed by molecular dynamics. Phys Rev B 2014;89(5). http://dx.doi.org/10.1103/PhysRevB.89.054309.

[24] Monachon C, Weber L, Dames C. Thermal boundary conductance: A materials science perspective. Annu Rev Mater Res 2016;46(1):433–63. http://dx.doi.org/10.1146/annurev-matsci-070115-031719.

[25] Qian X, Zhou J, Chen G. Phonon-engineered extreme thermal conductivity materials. Nature Mater 2021. http://dx.doi.org/10.1038/s41563-021-00918-3.

[26] Guo Y, Wang M. Phonon hydrodynamics and its applications in nanoscale heat transport. Phys Rep 2015;595:1–44. http://dx.doi.org/10.1016/j.physrep.2015.07.003.

[27] Chen G. Thermal conductivity and ballistic-phonon transport in the cross-plane direction of superlattices. Phys Rev B 1998;57(23):14958. http://dx.doi.org/10.1103/PhysRevB.57.14958.

[28] Maldovan M. Phonon wave interference and thermal bandgap materials. Nature Mater 2015;14(7):667–74. http://dx.doi.org/10.1038/nmat4308.

[29] Roy Chowdhury P, Shi J, Feng T, Ruan X. Prediction of Bi2Te3-Sb2Te3 interfacial conductance and superlattice thermal conductivity using molecular dynamics simulations. ACS Appl Mater Interfaces 2021;13(3):4636–42. http://dx.doi.org/10.1021/acsami.0c17851.

[30] Roy Chowdhury P, Reynolds C, Garrett A, Feng T, Adiga SP, Ruan X. Machine learning maximized Anderson localization of phonons in aperiodic superlattices. Nano Energy 2020;69:104428. http://dx.doi.org/10.1016/j.nanoen.2019.104428.

[31] Zhu F, Pan E, Qian Z, Wang Y. Dispersion curves, mode shapes, stresses and energies of SH and lamb waves in layered elastic nanoplates with surface/interface effect. Internat J Engrg Sci 2019;142:170–84. http://dx.doi.org/10.1016/j.ijengsci.2019.06.003.

[32] Farajpour A, Ghayesh MH, Farokhi H. A review on the mechanics of nanostructures. Internat J Engrg Sci 2018;133:231–63. http://dx.doi.org/10.1016/j.ijengsci.2018.09.006.

[33] Ogilvy JA. Wave scattering from rough surfaces. Rep Progr Phys 1987;50(12):1553–608. http://dx.doi.org/10.1088/0034-4885/50/12/001.

[34] Landauer R. Spatial variation of currents and fields due to localized scatterers in metallic conduction. IBM J Res Dev 1957;1(3):223–31. http://dx.doi.org/10.1147/rd.13.0223.

[35] Nazarov Y, Nazarov Y, Blanter Y. Quantum Transport: Introduction To Nanoscience. Cambridge University Press; 2009.

[36] Wilson RB, Cahill DG. Experimental validation of the interfacial form of the wiedemann-franz law. Phys Rev Lett 2012;108(25):255901. http://dx.doi.org/10.1103/PhysRevLett.108.255901.

[37] Koh YR, Shi J, Wang B, Hu R, Ahmad H, Kerdsongpanya S, et al. Thermal boundary conductance across epitaxial metal/sapphire interfaces. Phys Rev B 2020;102:205304. http://dx.doi.org/10.1103/PhysRevB.102.205304.

[38] Chen G. Nanoscale energy transport and conversion: A parallel treatment of electrons, molecules, phonons, and photons. Oxford University Press; 2005.

[39] Siemens ME, Li Q, Yang R, Nelson KA, Anderson EH, Murnane MM, et al. Quasiballistic thermal transport from nanoscale interfaces observed using ultrafast coherent soft X-ray beams. Nature Mater 2010;9(1):26–30. http://dx.doi.org/10.1038/nmat2568.

[40] Achenbach J. Wave propagation in elastic solids. Amsterdam: North-Holland Publishing Company; 1973.

[41] Bass F, Fuks I. Wave scattering from statistically rough surfaces. Oxford: Pergamon; 1979.

[42] Maznev AA. Boundary scattering of phonons: Specularity of a randomly rough surface in the small-perturbation limit. Phys Rev B 2015;91(13). http://dx.doi.org/10.1103/PhysRevB.91.134306.

[43] Berry MV. Nature's optics and our understanding of light. Contemp Phys 2015;56(1):2–16. http://dx.doi.org/10.1080/00107514.2015.971625.

[44] Shi F, Lowe M, Craster R. Diffusely scattered and transmitted elastic waves by random rough solid-solid interfaces using an elastodynamic kirchhoff approximation. Phys Rev B 2017;95(21):214305. http://dx.doi.org/10.1103/PhysRevB.95.214305.

[45] Shi F, Lowe MJS, Xi X, Craster RV. Diffuse scattered field of elastic waves from randomly rough surfaces using an analytical Kirchhoff theory. J Mech Phys Solids 2016;92:260–77. http://dx.doi.org/10.1016/j.jmps.2016.04.003.

[46] Lim J, Hippalgaonkar K, Andrews SC, Majumdar A, Yang P. Quantifying surface roughness effects on phonon transport in silicon nanowires. Nano Lett 2012;12(5):2475–82. http://dx.doi.org/10.1021/nl3005868.

[47] Liu B, Khvesyuk VI. Analytical model for thermal boundary conductance based on elastic wave theory. Int J Heat Mass Transfer 2020;159:120117. http://dx.doi.org/10.1016/j.ijheatmasstransfer.2020.120117.

[48] Little W. The transport of heat between dissimilar solids at low temperatures. Can J Phys 1959;37(3):334–49. http://dx.doi.org/10.1139/p59-037.

[49] Weber W. Adiabatic bond charge model for the phonons in diamond, Si, Ge, and α-Sn. Phys Rev B 1977;15(10):4789–803. http://dx.doi.org/10.1103/PhysRevB.15.4789.

[50] Gilat G, Nicklow RM. Normal vibrations in aluminum and derived thermodynamic properties. Phys Rev 1966;143(2):487–94. http://dx.doi.org/10.1103/PhysRev.143.487.

[51] Martinez M, Cardani L, Casali N, Cruciani A, Pettinari G, Vignati M. Measurements and simulations of athermal phonon transmission from silicon absorbers to aluminum sensors. Phys Rev A 2019;11(6):064025. http://dx.doi.org/10.1103/PhysRevApplied.11.064025.

[52] Gorham CS, Hattar K, Cheaito R, Duda JC, Gaskins JT, Beechem TE, et al. Ion irradiation of the native oxide/silicon surface increases the thermal boundary conductance across aluminum/silicon interfaces. Phys Rev B 2014;90(2):024301. http://dx.doi.org/10.1103/PhysRevB.90.024301.

[53] Ih Choi W, Kim K, Narumanchi S. Thermal conductance at atomically clean and disordered silicon/aluminum interfaces: A molecular dynamics simulation study. J Appl Phys 2012;112(5). http://dx.doi.org/10.1063/1.4748872.

[54] Minnich AJ, Chen G, Mansoor S, Yilbas BS. Quasiballistic heat transfer studied using the frequency-dependent Boltzmann transport equation. Phys Rev B 2011;84(23):235207. http://dx.doi.org/10.1103/PhysRevB.84.235207.

[55] Ran X, Guo Y, Wang M. Interfacial phonon transport with frequency-dependent transmissivity by Monte Carlo simulation. Int J Heat Mass Transfer 2018;123:616–28. http://dx.doi.org/10.1016/j.ijheatmasstransfer.2018.02.117.

[56] Khvesyuk VI, Liu B, Barinov AA. A new approach to calculation of the kapitza conductance between solids. Tech Phys Lett 2020;46(10):983–7. http://dx.doi.org/10.1134/S1063785020100065.

[57] Cheaito R, Gaskins JT, Caplan ME, Donovan BF, Foley BM, Giri A, et al. Thermal boundary conductance accumulation and interfacial phonon transmission: Measurements and theory. Phys Rev B 2015;91(3):035432. http://dx.doi.org/10.1103/PhysRevB.91.035432.

[58] Grafarend EW. Linear and nonlinear models: Fixed effects, random effects, and mixed models. de Gruyter; 2006.

[59] Ziman JM. Electrons and phonons: The theory of transport phenomena in solids. Oxford University Press; 1960.

[60] Dames C, Chen G. Theoretical phonon thermal conductivity of Si/Ge superlattice nanowires. J Appl Phys 2004;95(2):682–93. http://dx.doi.org/10.1063/1.1631734.

[61] Sun H, Pipe KP. Perturbation analysis of acoustic wave scattering at rough solid-solid interfaces. J Appl Phys 2012;111(2):023510. http://dx.doi.org/10.1063/1.3676250.

[62] Hua C, Chen X, Ravichandran NK, Minnich AJ. Experimental metrology to obtain thermal phonon transmission coefficients at solid interfaces. Phys Rev B 2017;95(20):205423. http://dx.doi.org/10.1103/PhysRevB.95.205423.

[63] Minnich AJ, Johnson JA, Schmidt AJ, Esfarjani K, Dresselhaus MS, Nelson KA, et al. Thermal conductivity spectroscopy technique to measure phonon mean free paths. Phys Rev Lett 2011;107(9):095901. http://dx.doi.org/10.1103/PhysRevLett.107.095901.

[64] Lu Z, Chaka AM, Sushko PV. Thermal conductance enhanced via inelastic phonon transport by atomic vacancies at Cu/Si interfaces. Phys Rev B 2020;102(7):075449. http://dx.doi.org/10.1103/PhysRevB.102.075449.

[65] Shi J, Yang X, Fisher TS, Ruan X. Dramatic increase in the thermal boundary conductance and radiation limit from a nonequilibrium Landauer approach. 2019, URL https://arxiv.org/abs/1812.07910.

[66] Simkin MV, Mahan GD. Minimum thermal conductivity of superlattices. Phys Rev Lett 2000;84(5):927–30. http://dx.doi.org/10.1103/PhysRevLett.84.927.

[67] Costescu RM, Wall MA, Cahill DG. Thermal conductance of epitaxial interfaces. Phys Rev B 2003;67(5). http://dx.doi.org/10.1103/PhysRevB.67.054302.

[68] Duda JC, Yang C-YP, Foley BM, Cheaito R, Medlin DL, Jones RE, et al. Influence of interfacial properties on thermal transport at gold:silicon contacts. Appl Phys Lett 2013;102(8):081902. http://dx.doi.org/10.1063/1.4793431.

[69] Luckyanova MN, Garg J, Esfarjani K, Jandl A, Bulsara MT, Schmidt AJ, et al. Coherent phonon heat conduction in superlattices. Science 2012;338(6109):936–9. http://dx.doi.org/10.1126/science.1225549.

[70] Ravichandran J, Yadav AK, Cheaito R, Rossen PB, Soukiassian A, Suresha S, et al. Crossover from incoherent to coherent phonon scattering in epitaxial oxide superlattices. Nature Mater 2014;13(2):168–72. http://dx.doi.org/10.1038/nmat3826.

[71] Zhang Z, Guo Y, Bescond M, Chen J, Nomura M, Volz S. Coherent thermal transport in nano-phononic crystals: An overview. APL Mater 2021;9(8):081102. http://dx.doi.org/10.1063/5.0059024.

[72] Zhang Y, Seghete D, Abdulagatov A, Gibbs Z, Cavanagh A, Yang R, et al. Investigation of the defect density in ultra-thin Al2O3 films grown using atomic layer deposition. Surf Coat Technol 2011;205(10):3334–9. http://dx.doi.org/10.1016/j.surfcoat.2010.12.001.

[73] Persson BNJ, Lorenz B, Volokitin AI. Heat transfer between elastic solids with randomly rough surfaces. Eur Phys J E 2010;31(1):3–24. http://dx.doi.org/10.1140/epje/i2010-10543-1.

[74] Majumdar A, Reddy P. Role of electron–phonon coupling in thermal conductance of metal–nonmetal interfaces. Appl Phys Lett 2004;84(23):4768–70. http://dx.doi.org/10.1063/1.1758301.

[75] Sadasivam S, Waghmare UV, Fisher TS. Electron-phonon coupling and thermal conductance at a metal-semiconductor interface: First-principles analysis. J Appl Phys 2015;117(13):134502. http://dx.doi.org/10.1063/1.4916729.

[76] Lyeo H-K, Cahill DG. Thermal conductance of interfaces between highly dissimilar materials. Phys Rev B 2006;73:144301. http://dx.doi.org/10.1103/PhysRevB.73.144301.

[77] Feng T, Zhong Y, Shi J, Ruan X. Unexpected high inelastic phonon transport across solid-solid interface: Modal nonequilibrium molecular dynamics simulations and Landauer analysis. Phys Rev B 2019;99:045301. http://dx.doi.org/10.1103/PhysRevB.99.045301.

[78] Miao W, Wang M. Reexamination of electron-phonon coupling constant in continuum model by comparison with Boltzmann transport theory. Int J Heat Mass Transfer 2021;174:121309. http://dx.doi.org/10.1016/j.ijheatmasstransfer.2021.121309.

[79] Miao W, Wang M. Nonequilibrium effects on the electron-phonon coupling constant in metals. Phys Rev B 2021;103(12):125412. http://dx.doi.org/10.1103/PhysRevB.103.125412.